Journal of Remote Sensing
A SCIENCE PARTNER JOURNAL

RESEARCH ARTICLE

Spatial and Temporal Variations of Thermal Contrast in the Planetary Boundary Layer

Tommaso Di Gioacchino[1], Lieven Clarisse[1*], Lara Noppen[1], Martin Van Damme[1,2], Sophie Bauduin[1], and Pierre Coheur[1]

[1]Spectroscopy, Quantum Chemistry and Atmospheric Remote Sensing (SQUARES), Université Libre de Bruxelles (ULB), Brussels, Belgium. [2]Royal Belgian Institute for Space Aeronomy, Brussels, Belgium.

*Address correspondence to: Lieven.Clarisse@ulb.be

Citation: Di Gioacchino T, Clarisse L, Noppen L, Van Damme M, Bauduin S, Coheur P. Spatial and Temporal Variations of Thermal Contrast in the Planetary Boundary Layer. *J. Remote Sens.* 2024;4:Article 0142. https://doi.org/10.34133/remotesensing.0142

Submitted 16 November 2023
Accepted 25 March 2024
Published 21 May 2024

High-spectral resolution infrared sounders on board satellites can measure atmospheric trace gases confined to the planetary boundary layer (PBL). However, their sensitivity to the PBL depends on the temperature difference between the surface and the atmosphere, the so-called thermal contrast (TC). After reviewing the physical aspects of TC and how it drives measurement sensitivity, we characterize the global and temporal behavior of TC in clear-sky conditions. Combining land surface temperatures from the Copernicus Global Land Services dataset with air temperatures from the European Centre for Medium-Range Weather Forecasts reanalysis v5, we obtain global monthly averages of TC at high spatial (31 km) and temporal (1 h) resolution. TCs are analyzed as a function of time of the day, time of the year, location and land cover. Daytime maxima are observed from 1130 to 1330 local time, from 5–10 K in winter to 10–30 K in summer. A large dependency on land cover type is observed, both in the magnitude of the daily variations, and in the seasonality. For bare soils, shrublands, sparse and herbaceous vegetation, a maximum is seen in summer with daily TC amplitudes over 30 K. In contrast, for forests, wetlands, and croplands, the seasonal maximum occurs in spring, with daily variations below 15 K. Nighttime TCs typically range between −5 and −10 K. Occasionally, very favorable nighttime measurement conditions occur during winter and autumn due to large temperature inversions. Throughout the paper, we illustrate important concepts by means of satellite observations of NH_3 over the Po Valley (Italy).

Introduction

Satellite remote sensing has become invaluable for monitoring the global emissions of several key pollutants. Improved sounding technology combined with algorithmic advances have in particular enabled quantifying the world's largest localized emissions point sources (e.g., power plants, petrochemical plants, mining operations, and animal farms [1]). This was achieved both with sounders measuring solar reflected light and with those measuring the Earth's outgoing longwave infrared radiation. The former are sensitive to point sources of, e.g., nitrogen dioxide (NO_2) [2], sulfur dioxide (SO_2) [3], and methane (CH_4) [4], while the latter can be used to measure emission sources of, e.g., sulfur dioxide (SO_2) [5,6], carbon monoxide (CO) [7,8], ammonia (NH_3) [9,10], and ethylene (C_2H_4) [11].

Except for the emissions from aircraft or very tall industrial chimneys, most anthropogenic pollutants are released in the planetary boundary layer (PBL), which is the lower-most part of the troposphere characterized by rapid vertical mixing [12]. Its height varies typically between 25–250 m (at night) and 250–2,500 m (during daytime). The PBL is unfortunately the atmospheric layer to which satellite sounders have the least sensitivity. This is particularly true for sounders measuring in the infrared spectral domain, whose sensitivity is primarily driven by the thermal contrast (TC), which is the temperature difference between the surface and that of the atmosphere [5,7,8,13–18]. Because the temperature of the atmosphere generally decreases with altitude in the troposphere, sensitivity generally increases with altitude. Near the surface, TC mainly originates from the different cooling and heating rates between the surface and atmosphere. TC is usually positive during daytime, while at night it turns negative, possibly enhanced by low-level temperature inversions [8,13]. Both situations provide infrared measurement sensitivity to the PBL, but the daytime typically provides the best conditions, as the TC in absolute value is usually larger during daytime than at night [7,15].

It is known that TC varies as a function of time of the day, time of the year, location, and surface type [19–21]. However, up to now, no study has characterized in detail the spatiotemporal variations of the TC with respect to the altitudes most relevant to infrared remote sensing. Given the growing importance of infrared sounders for measuring boundary layer pollutants, understanding the statistical behavior of TC is essential. Here, we combine the Copernicus Global Land Services land surface temperature (LST) dataset, derived from geostationary satellite measurements, with air temperatures from the European Centre for Medium-Range Weather Forecasts (ECMWF) reanalysis v5 (ERA5) [22] to obtain a global, yearlong, TC dataset at high temporal (1 h) and high spatial (31 km) resolution. We report TCs at 3 different altitudes: at the standard meteorological height of

2 m, at half the PBL height, and at the height corresponding to the maximum temperature of the lower troposphere. As the LSTs are derived from direct satellite observations, both this dataset and our derived TC datasets are representative of clear-sky conditions. We refer to [19–23] for a discussion of TC in cloudy conditions. The TC datasets presented and analyzed in this paper are made publicly available and have numerous applications. They can be used to provide constraints on the time windows and boundary conditions (e.g., land cover type) for which the sensitivity of thermal infrared instruments is best. It also allows determining the most favorable overpass time for polar orbiting infrared sounders or the organization of airborne measurement campaigns for near-surface pollutants. Finally, this unique dataset can be used to statistically assess the measurement sensitivity of current and future infrared sounders.

In the next section, we recall the notion of TC and explain how it drives sensitivity in the thermal infrared. We also present a detailed example of a diel TC cycle. Materials and Methods presents the different data and methods that were used to build the TC dataset. In Analysis, we present and analyze a variety of different statistics summarizing the global spatiotemporal behavior of TC. Conclusions summarizes the main results of this study.

TC and radiative effects

Consider a surface that emits a radiance $I_s(\nu)$ at wavenumber ν. After passage through an isothermal nondiffusive atmospheric layer at a temperature T_a, the observed radiance $I_{\text{obs}}(\nu)$ can be written as [24]

$$I_{\text{obs}}(\nu) = I_s(\nu)t_\nu + B\big(T_a,\nu\big)\big(1-t_\nu\big) \tag{1}$$

$$= I_s(\nu)\big(1-a_\nu\big) + B\big(T_a,\nu\big)a_\nu, \tag{2}$$

with t_ν the transmittance and $a_\nu = 1 - t_\nu$, the absorptivity of the layer. Both depend on the composition of the air in the layer. $B(T,\nu)$ is Planck's blackbody function. Introducing a wavenumber-dependent brightness temperature of the surface $T_b(\nu)$ such that $I_s(\nu) = B(T_b,\nu)$ and observed brightness temperature $T_{\text{obs}}(\nu)$ such that $I_{\text{obs}}(\nu) = B(T_{\text{obs}},\nu)$, we can rewrite Eq. 2 as

$$B\big(T_{\text{obs}},\nu\big) = B\big(T_b,\nu\big)\big(1-a_\nu\big) + B\big(T_a,\nu\big)a_\nu, \tag{3}$$

or as

$$B\big(T_b,\nu\big) - B\big(T_{\text{obs}},\nu\big) = \big(B\big(T_b,\nu\big) - B\big(T_a,\nu\big)\big)a_\nu. \tag{4}$$

From Eq. 3 and $0 \le a_\nu \le 1$ follows that the observed brightness temperature lies between the brightness temperature of the surface and that of the layer. As expected, when a_ν tends to zero, the observed temperature $T_{\text{obs}}(\nu)$ tends toward the surface brightness temperature T_b. Conversely, when a_ν tends to one, the layer is opaque and only the layer radiation is observed: $T_{\text{obs}}(\nu) = T_a$. We also see that in the absence of TC (TC = $T_b(\nu) - T_a = 0$), the observed temperature equals the brightness temperature of the layer and the surface ($T_{\text{obs}}(\nu) = T_a = T_b(\nu)$), and the measurement is insensitive to the amount of absorption within the layer.

The left term of Eq. 4 can be interpreted as the spectral change in channel ν with and without the air layer present. The right term of the equation shows that this change equals the absorptivity of the layer times the TC expressed in radiances ($\text{TC}_R = B(T_b,\nu) - B(T_a,\nu)$). In other words, the measured signal strength is the product of the radiance TC with a factor that depends on the gas amount. Hence, the importance of TC in the infrared. We also see from Eq. 4 that when TC is positive, the observed temperature is lower than the brightness temperature of the surface: $T_{\text{obs}}(\nu) < T_b(\nu)$. This results in spectral absorption features in the observed spectrum. Conversely, when the TC is negative, we have $T_{\text{obs}}(\nu) > T_b(\nu)$ and spectral emission features are observed in the spectrum.

This contrasting behavior is illustrated in Fig. 1, which shows 2 spectra observed by the Infrared Atmospheric Sounding Interferometer (IASI) [25] over the Po Valley (Italy). The spectra were selected based on their large NH_3 signatures. The spectrum in Fig. 1A was measured in the morning in late spring 2021. Across the 780- to 1,230-cm^{-1} range, we observe absorption lines and broader absorption features of H_2O, O_3, CO_2 and NH_3. The TC at the time of the observation was 12.2 K (with respect to half the PBL). Figure 1B shows a nighttime spectrum observed in the winter. A particularly large negative TC of −9.5 K gives rise to NH_3 emission features, which are best seen near 930.75 and 967.25 cm^{-1}. The fact that the direction (absorption or emission) of the spectral features agrees with the sign of the TC in the PBL, is consistent with NH_3 being mostly confined to the PBL as a short-lived species. Water vapor is present throughout the troposphere, and the strong water vapor lines seen in the springtime spectrum are highly reduced in magnitude in wintertime. This is due to: (a) reduced TC (with respect to the entire lower troposphere), (b) a cancellation effect of emission in the boundary layer with absorption higher up, and (c) overall lower H_2O concentrations during winter. For the strongest H_2O lines, emission is seen in the wings (especially notable in the 1,170- to 1,230-cm^{-1} range), a radiative transfer effect that has also been observed for CO [8]. The O_3 absorption feature (990 to 1,070 cm^{-1}) is largely unaffected by negative TC in the PBL, as the observed O_3 spectral signatures originate mostly from the upper troposphere and lower stratosphere.

To conclude this section, we note that the detection threshold of a sounder to a specific trace gas is inversely proportional to the radiance TC. This can be deduced from Eq. 4. Assuming small trace amounts of the gaseous absorber of interest, the absorptivity is proportional to its total column X. Equating the sensor-dependent minimal detectable radiance perturbation $\Delta R(\nu)$ with the observed signal $B(T_b,\nu) - B(T_{\text{obs}},\nu)$, we then see that the minimum amount of trace gas X_{min} that can be detected can be written as

$$X_{\text{min}} \propto \frac{\Delta R(\nu)}{|B\big(T_b,\nu\big) - B\big(T_a,\nu\big)|}. \tag{5}$$

This relation, as a function of TC, is illustrated in Fig. 2. We observe clearly the increased sensitivity for both negative and positive TC and the blind spot at zero TC. To remove the dependence on $\Delta R(\nu)$, the y-axis is expressed relative to the value at TC = 5 K. We find a normalized detection threshold of 5 at TC = 1 K, 0.49 at TC = 10 K, and 0.23 at TC = 20 K.

TC in the PBL, an example

Figure 3B and C shows the diel cycle of the surface, air temperature, and TC as observed during a day in March in the Po Valley (Italy). TC is expressed with respect to: (a) a height of 2 m (yellow), which is a representative height for pollutants

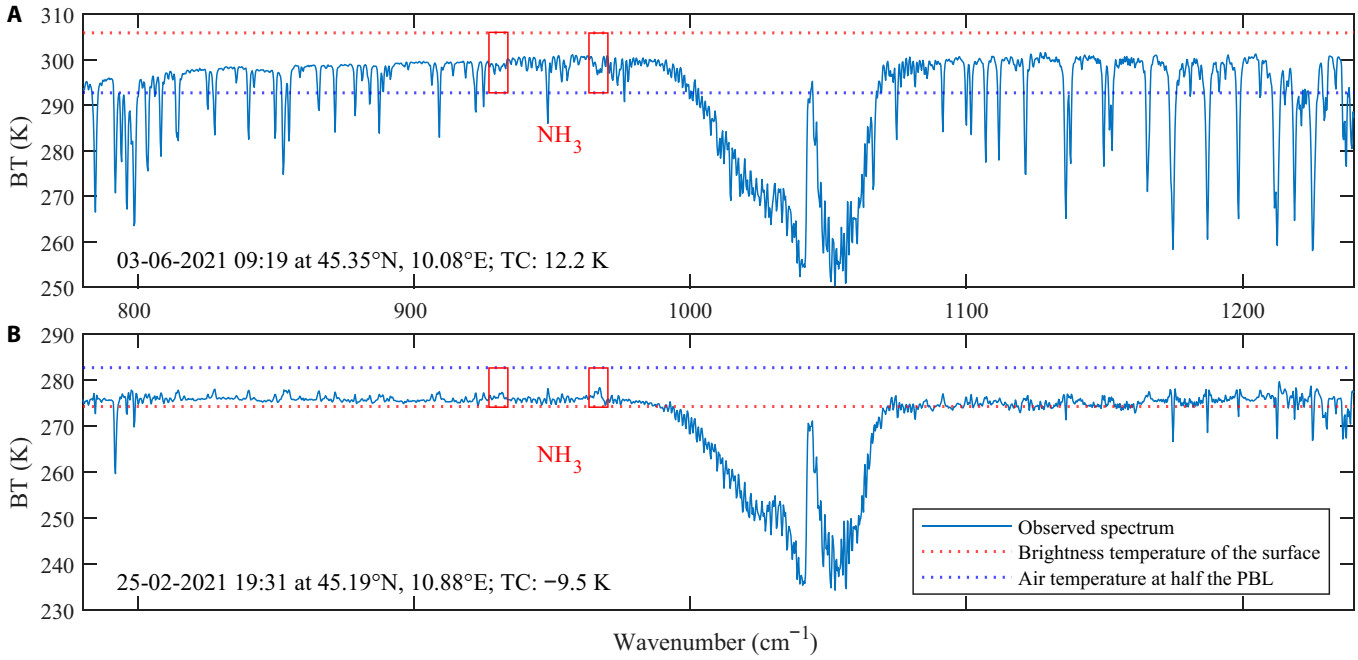

Fig. 1. IASI spectra (blue) observed over the Po Valley (Italy) in spring (A) and winter (B). The brightness temperature of the surface (dotted red) and air temperature at half the PBL (dotted blue) at the time of the measurement show the magnitude and sign of the TC. The spring spectrum shows absorption features corresponding to a positive TC. Conversely, the winter spectrum shows emissions features during negative TC conditions. The spectral ranges where NH_3 is best observed are highlighted in red around 930.75 and 967.25 cm^{-1}.

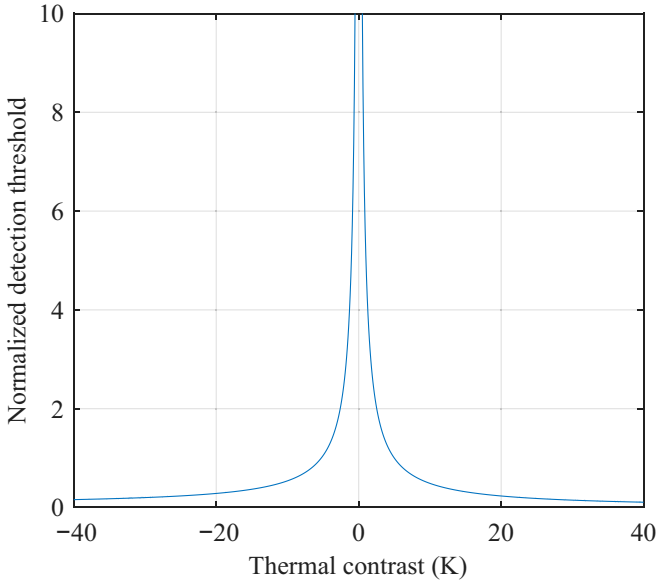

Fig. 2. Relation between TC and the detection threshold normalized at 5 K.

located at the surface (b) half of the PBL (PBL/2, green), which is a representative height for pollutants in a well-mixed boundary layer, and (c) the height corresponding to the maximum lower tropospheric temperature (MaxT, blue). The latter gives a lower bound on the TC (i.e., TC at any other altitude is larger). In typical daytime conditions (positive TC), this height corresponds to the location with the lowest sensitivity, while at night (negative TC), it corresponds to the location of the highest sensitivity.

We can see from Fig. 3 that after sunrise, the surface warms up more quickly than the air. This is because it absorbs solar radiation more efficiently [7]. With some delay, the solar energy is transferred from the surface to the atmosphere via conduction, convection, evapotranspiration, and (infrared) radiation. This results in an increase in TC at each reference height until mid-afternoon. The heating of the atmosphere goes hand in hand with the formation and expansion of an unstable (convective) PBL. Because of the change in reference height, the air temperature at half the PBL undergoes the smallest change throughout the day. The TC with respect to this temperature therefore closely follows the daily cycle of the surface temperature, with a maximum around or just after noon. In the early afternoon, the surface starts cooling down slowly, while the air temperature still rises. By as early as 1600, this leads to a negative TC at 2 m. After a delay of 2 to 3 h, the air temperature also starts to decrease, together with the collapse of the boundary layer. The behavior observed here, i.e., a peak in surface temperature around noon followed by a peak in air temperature several hours later, has been noted to be quite typical for land surfaces [19]. From about 1600 until about 0800, all 3 TCs are negative. As seen in the vertical temperature profiles of Fig. 3A, from midnight until about 0400 in the morning, a strong temperature inversion is present at an altitude of about 100 m, amplifying the negative TC. This inversion is best seen in the TC calculated with respect to the maximum tropospheric temperature. This reference height is also commonly used to characterize the seasonality of boundary layer temperature inversions [26,27].

The example illustrates the typical intradaily patterns that are observed globally over land at tropical and mid latitudes. While the rest of the paper is focused on these regions, note that skin sea surface temperatures vary little throughout the

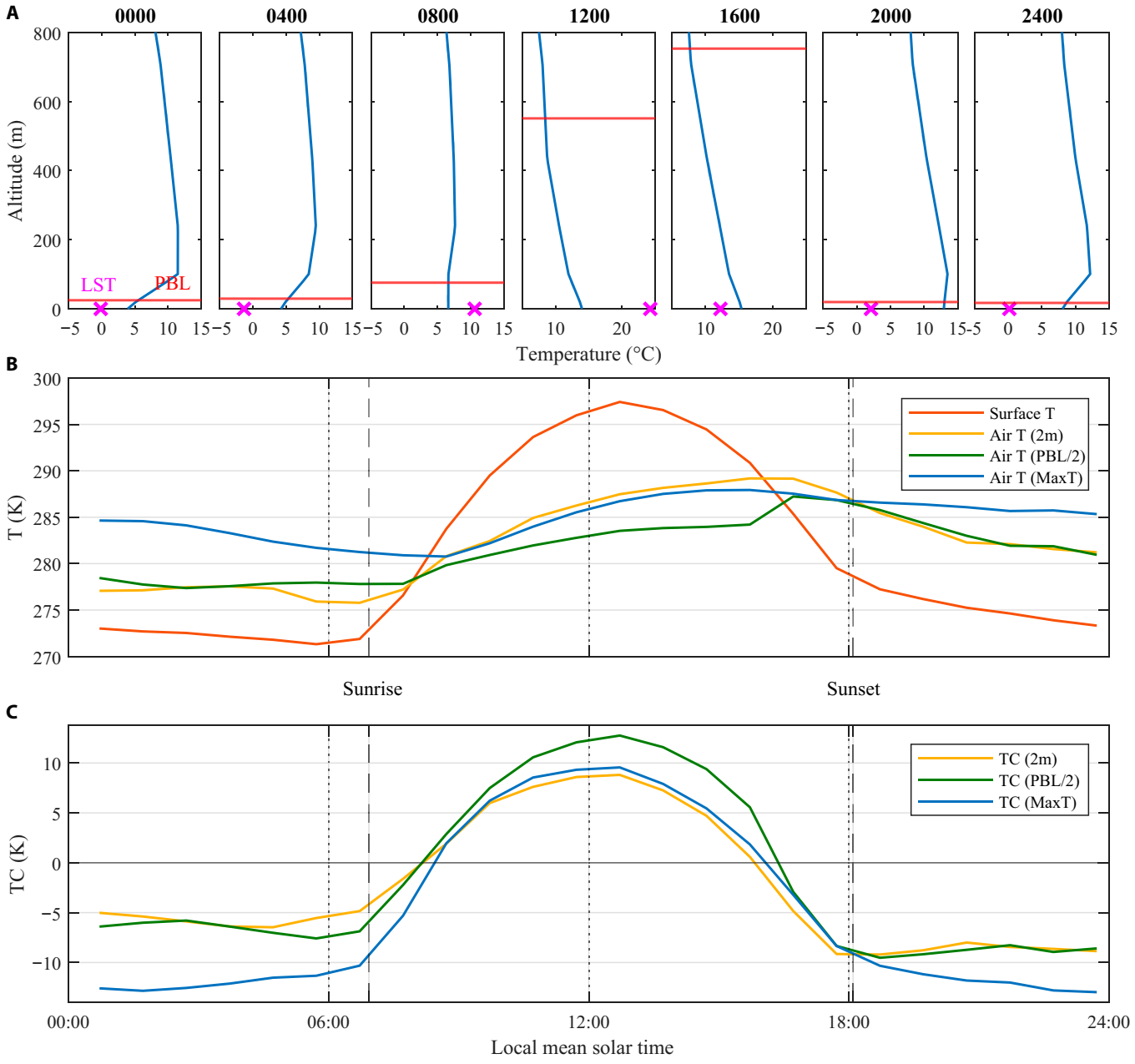

Fig. 3. The diel cycle of the TC over Mantua (Po Valley, Italy) on 2021 March 2. Panel (A) shows the vertical temperature profile (blue), the PBL height (red), and the LST (magenta) at 4-h intervals. Panel (B) shows the air temperature at 2 m (yellow), the air temperature at half the PBL (green), the air temperature at the height corresponding to the maximum tropospheric temperature (blue), and the surface temperature (red). Panel (C) shows the corresponding TCs. Note that for several hours, the maximum air temperature is erroneously lower than the temperature at 2 m. This is related to the fact that the ERA5 2m temperature is an independent product and not derived from the ERA5 temperature profile product.

day [28] so that TC is generally low over ocean. A notable exception is that of the transport of hot inland air over coastal areas, giving rise to strong negative TC [29]. At high latitudes, TCs are generally also low [19], except for the presence of strong temperature inversions. These occur especially in winter and can persist throughout the day and night. We refer to [5] for a detailed case study of infrared measurements of anthropogenic SO_2 emissions in Norilsk (Siberia).

As a final note, the TC at the maximum temperature, which was introduced in this section, has special interest in that it allows us to put strict bounds on retrieved gas abundances. These can be obtained, for instance, from a retrieval based on a 1-layer radiative transfer model (as in Eq. 4). Indeed, suppose we have a pollutant that is entirely confined to a thin atmospheric layer situated at the height of the maximum tropospheric temperature. When the TC is positive, the TC at this temperature is smaller than the TC calculated with respect to any other reference height. Consequently, the retrieved column obtained in this way is an upper bound for the actual column abundance. On the other hand, when TC is negative, the TC with respect to the maximum temperature is the most negative TC available, or the largest TC in absolute value. Hence,

retrieving the column with this TC yields a lower bound on the gas abundance at night.

Materials and Methods

Following the example presented in the last section, the global hourly dataset of TC presented in this paper relies on air temperatures from the ECMWF ERA5 reanalysis [22,30,31] at 3 different altitudes: the standard meteorological height of 2 m, half the PBL (the PBL height itself is also obtained from ERA5), and the height corresponding to the maximum temperature of the lower troposphere (within a maximum of 3 km). Hourly data were obtained at a regular grid of 0.28125° × 0.28125°, close to the ERA5 native N320 Gaussian grid. The spatiotemporal resolution of ERA5 is coarser than the other datasets used in this paper, and subsequently, all other datasets are regridded to match the resolution of ERA5 (see below).

Skin temperatures from 2021 January 18 to 2022 January 18 were obtained from the LST dataset [32,33]. This dataset is based on measurements from several geostationary satellites: Meteosat Second Generation satellites for Europe and Africa, Meteosat Second Generation Indian Ocean Data Coverage for the Middle East, Geostationary Operational Environmental Satellite East for North and South America, and finally Himawari for eastern Asia and Oceania. Note that high latitudes and oceans are not included. The original LST dataset at a horizontal resolution of 5 km was interpolated and averaged on the coarser ERA5 grid. Skin temperatures T_s were then converted to skin brightness temperatures T_b, taking into account the local surface emissivity ϵ_ν:

$$T_b(\nu) = B^{-1}\left(\epsilon_\nu B\left(T_s, \nu\right), \nu\right). \quad (6)$$

For a surface temperature of 300 K at 1,000 cm^{-1}, this equation shows that T_b is lower than T_s by some 1 to 5 K for emissivities between 0.92 and 0.98. Surface emissivity depends on land cover and was taken here from an IASI-derived monthly climatology [34]. From this, global distributions of TC were obtained for each day and each Coordinated Universal Time (UTC) hour. These daily, hourly maps were then averaged on a monthly basis to create a 4D matrix (latitude, longitude, month and UTC hour). However, these TC maps are difficult to analyze as a given UTC hour corresponds to a different local time depending on the location. For this reason, we interpolated and remapped the UTC-based monthly averaged maps to a fixed local mean solar time (LMST) with

$$\text{LMST} = \text{UTC} + \text{longitude} / 15. \quad (7)$$

The resulting 4D matrices, representing the various TCs at each reference height, comprise the publicly available dataset and form the basis for the subsequent analysis. The analysis presented in the rest of the paper primarily focuses on the TC with respect to half the PBL during daytime, and on the TC with respect to the maximum tropospheric temperature at night.

In what follows, we will see that there is a strong dependence of TC on the land cover. To conduct a quantitative analysis, we used the global 100-m land cover map [35] produced by Copernicus Land Service and derived from PROBA-V satellite observations and ancillary datasets. This land cover map consists of the 23 classes of UN-FAO's Land Cover Classification System [36]. We merged these into the 7 classes as illustrated in Fig. 4: (a) forest and wetland, (b) shrubland and herbaceous vegetation, (c) cropland, (d) built up, (e) bare and sparse vegetation, (f) permanent water bodies, (g) snow, ice, moss, and lichens. To aggregate months into seasons, 3 latitude zones were considered: (a) between 30°N and 60°N, broadly matching the northern temperate zone, (b) a tropical area, between 30°N and 30°S, and (c) between 30°S and 60°S. As a result, a smaller dataset was obtained with

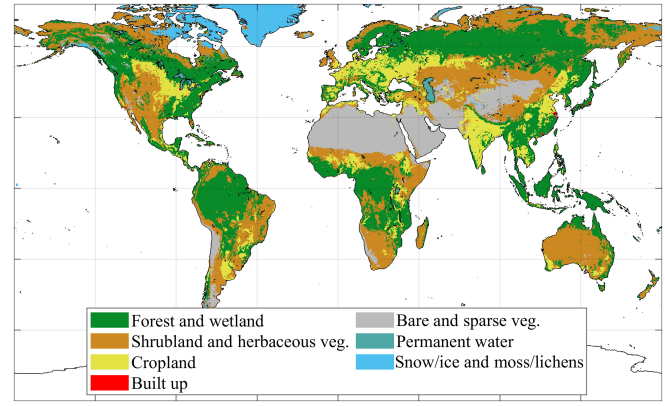

Fig. 4. Global distribution of the land cover used in the analysis. Compared to the original Copernicus land cover dataset, the number of classes was reduced from 23 to 7.

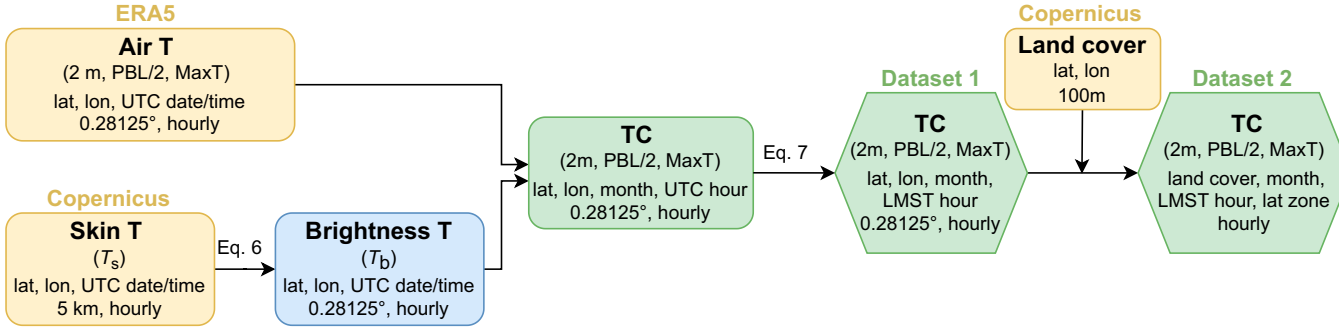

Fig. 5. Flowchart illustrating the data processing, with 3 main input datasets (ERA5, Copernicus land surfaces and Copernicus land cover) and 2 main TC datasets.

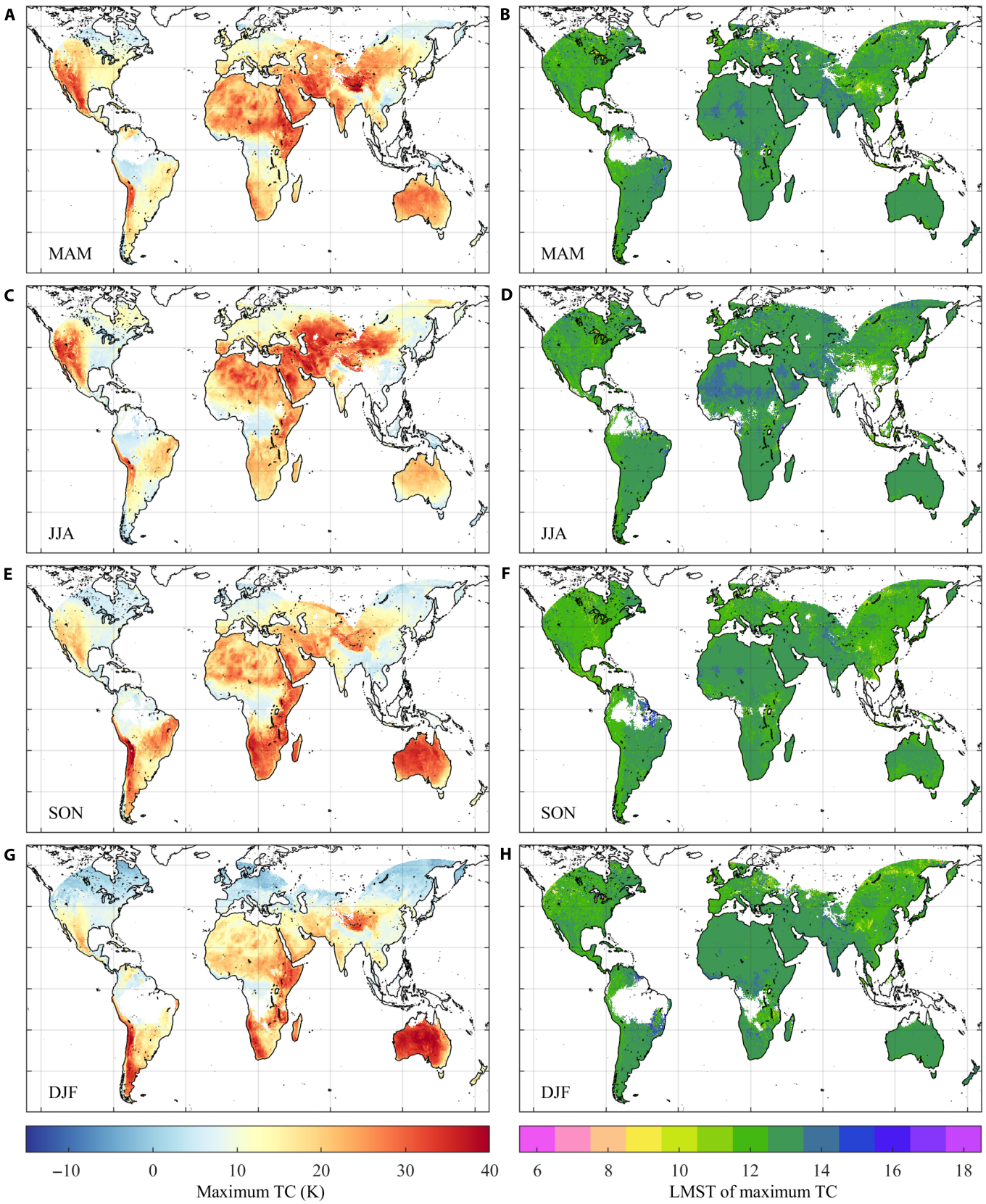

Fig. 6. The left panels (A, C, E, and G) show the global distribution of the mean maximum TC calculated at half the PBL, for each quarter of 2021. The right panels (B, D, F, and H) show the global distribution of the average LMST hour at which the maximum is reached. The quarters are abbreviated as March-April-May (MAM), JJA, September-October-November (SON) and December-January-February (DJF).

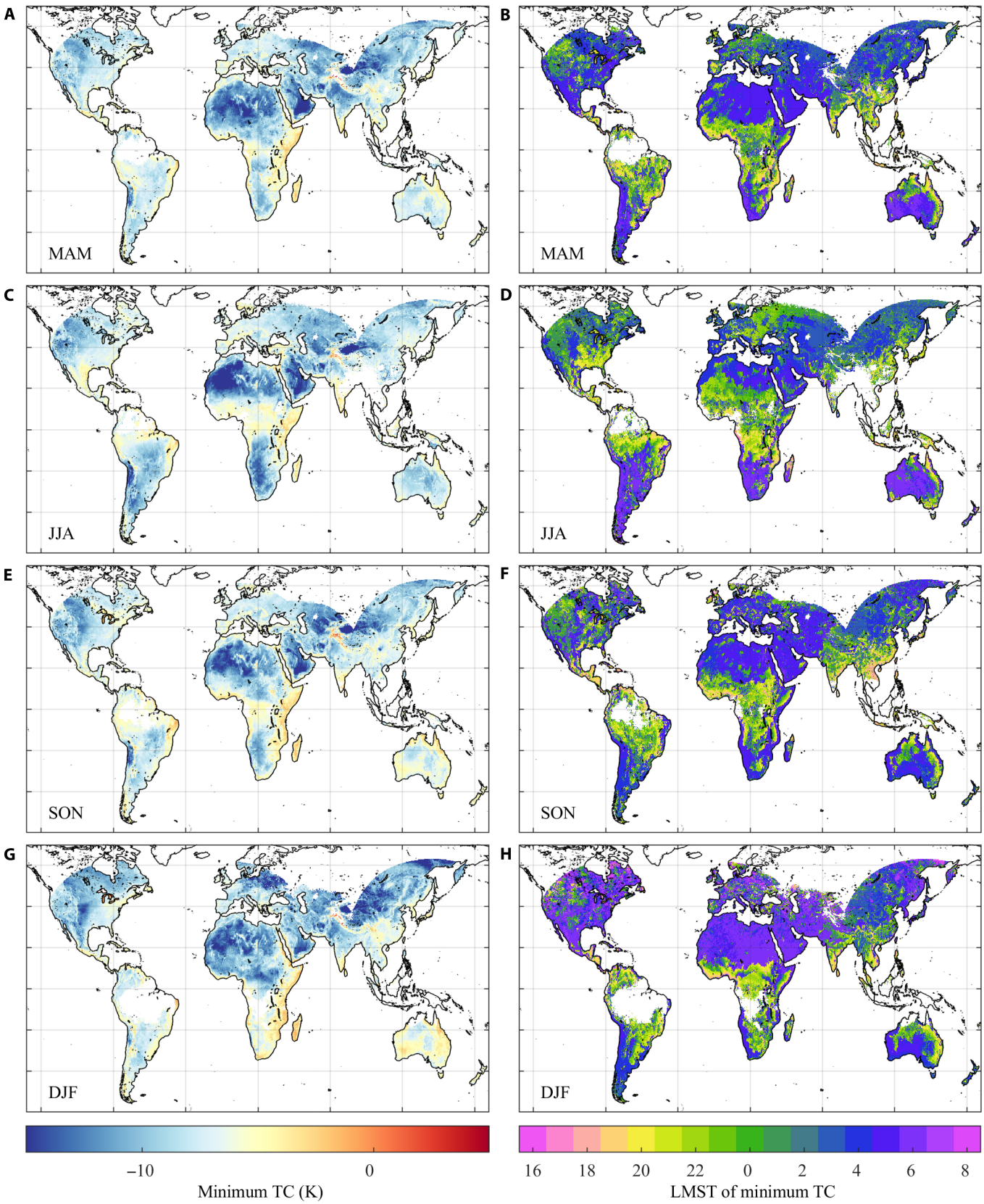

Fig. 7. The left panels (A, C, E, and G) show the global distribution of the mean minimum TC calculated at the height of the maximum temperature, for each quarter of 2021. The right panels (B, D, F, and H) show the global distribution of the average LMST hour at which the minimum is reached.

TC as a function of land cover type, latitudinal zone, month, and LMST. These data are also part of the publicly available dataset. A flowchart of the data processing is displayed in Fig. 5. All data manipulation (including interpolation and regridding), analysis and figure production was carried out with Matlab 2023b software.

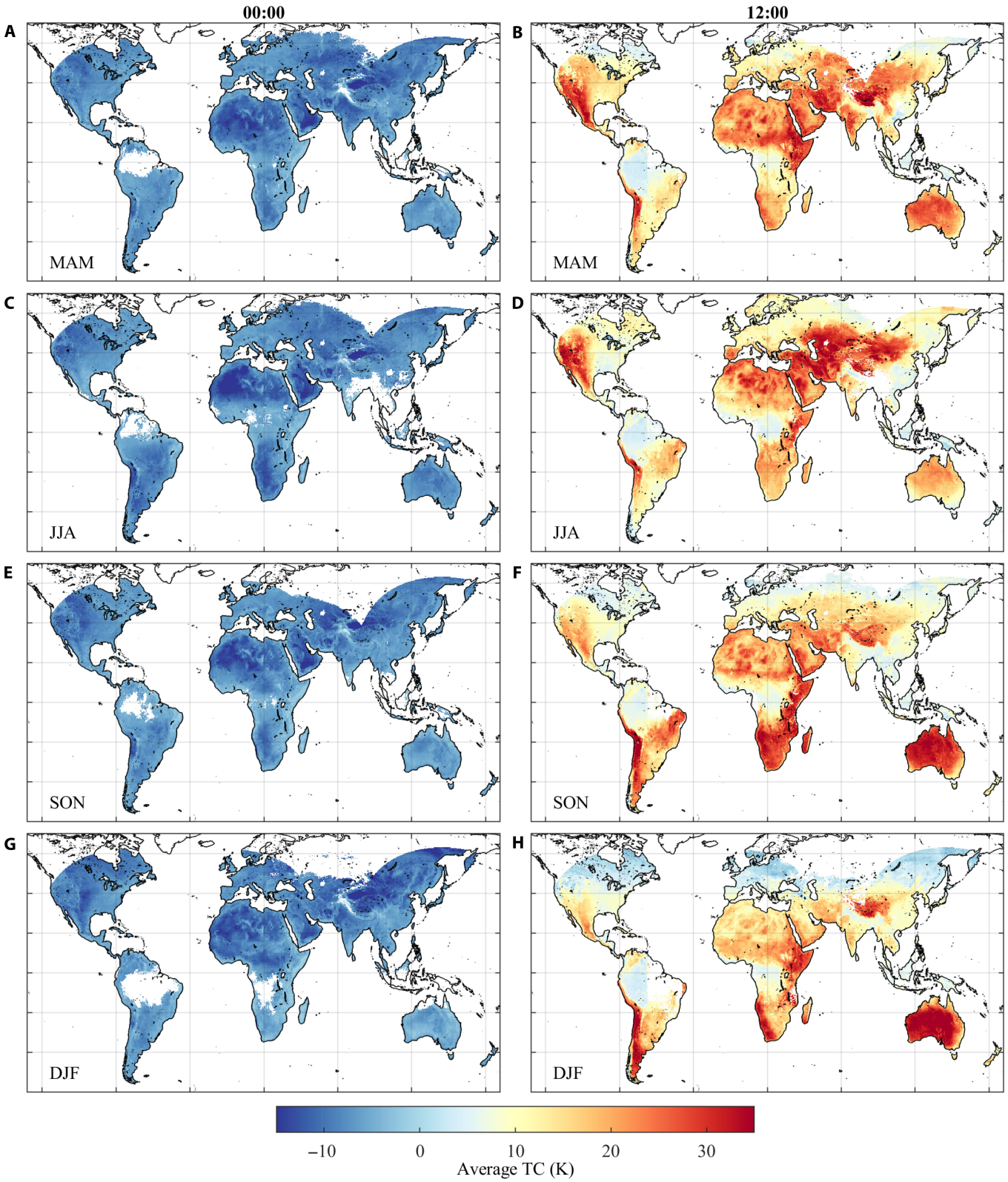

Fig. 8. The left panels (A, C, E, and G) show the average global distribution of TC calculated at 0000 LMST for the reference height of the maximum temperature of the lower troposphere, for each quarter of 2021. The right panels (B, D, F, and H) show the average global distribution of TC measured at half the PBL at 1200 LMST for the same 3-month periods.

Results

Seasonal distributions

Based on the seasonal averages, the LMST for which the TC reaches the maximum and minimum was found for each spatial grid cell. The result is shown in Fig. 6 for the maximum and Fig. 7 for the minimum. The white patches on these maps are related to cloud cover (e.g., over the Amazon forest) or the limited coverage of the satellite measurements on which the LST dataset is based (e.g., over the northern latitudes).

The maxima were calculated with the reference height for the air temperature at half the PBL. They reveal marked spatial and seasonal variability, ranging from around 0 K TC at high latitudes in the winter to over 40 K at selected locations in the spring and summer. This is consistent with the seasonality of the TC with respect to the air at 2 m, reported in [19]. Comparing the land cover map of Fig. 4 with Fig. 6 shows that TC is highly correlated with the surface type. We will come back to this in Land cover type. The time at which this maximum is reached consistently falls between 1030 and 1430 LMST, with the majority of maxima occurring between 1130 and 1330. This timing can be linked to the maxima of the LST, which are typically reached around noon, coinciding with maxima in solar radiation [19,21]. From the discussion in Radiative effects, this suggests that these time windows provide the best measurement conditions in the infrared during daytime. During the winter months, large parts of the world, particularly at northern latitudes, exhibit average maxima near or below zero.

Similar distributions for the minima at the reference height corresponding to the maximum tropospheric temperature are shown in Fig. 7. They exhibit much less variability than the maxima, both seasonally and spatially with a seasonal average starting from around −15 to 0 K. The time at which this minimum is reached on the other hand varies much more than for the maximum, from approximately 1830 to 0830 in the morning, with spatial patterns influenced by surface emissivity and the inland distance from sea. This larger variability has been noted before in [19]. Excluding areas with bare and sparse vegetation, such as deserts, we find that TC minima below −10 K are primarily observed during the winter season (July to August or December to February depending on the hemisphere). In winter, it is more common for these minima to occur in the early morning.

Figure 8 displays the seasonal average TCs at 0000 and 1200 LMST. These maps can be used as reference for the sensitivity of a polar orbiting instrument with an overpass time at local noon and midnight. The maps at noon highlight the large variability of daytime TC, both as a function of place and time, leading to large variations in boundary layer measurement sensitivity. The influence of surface elevation on TC, with higher altitudes exhibiting lower TCs (e.g., over the Tibetan plateau), can also be seen. At midnight, the persistence of negative TC values implies, at least in principle, measurement sensitivity to some part of the lowermost atmospheric layer.

Land cover type

The previous subsection demonstrated that TC strongly depends on location. Here, we explore further the temporal variability of TC in relation to land cover types, focusing on the latitudinal region between 30°N and 60°N, to ease interpretation of the seasonal dependence. The results are presented in Figs. 9 to 12. Note that in these figures, we do not show the land cover types of permanent water bodies (mainly represented by the Great Lakes

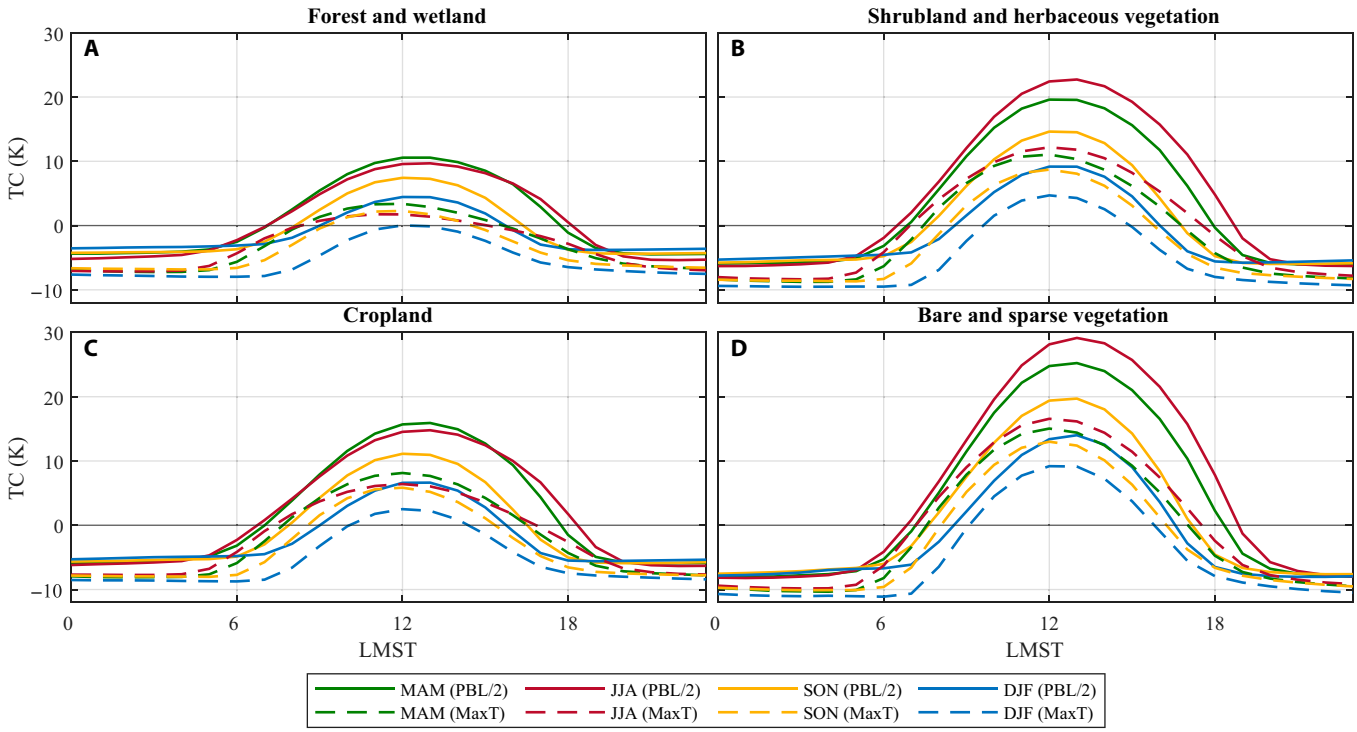

Fig. 9. Diel cycle of TC for different land cover types (A to D) in the northern temperate zone averaged over 3-month periods. The solid lines show the TC calculated at half the PBL, whereas the dashed lines show the TC calculated at the height corresponding to the maximum temperature of the lower troposphere.

and the Caspian Sea) and built up areas. These were excluded as the interpretation of their average TC values is hampered by their uneven global distribution and as these land cover types are often contaminated with other land cover types because of their small spatial extent.

Figure 9 presents the seasonally averaged diel cycles of TC for different land cover types. The TC measured at half the PBL (solid lines) consistently peaks at around 1200 or 1300 LMST across all land cover types and seasons. Daytime TC maxima in summer and spring are nearly double those in winter. In

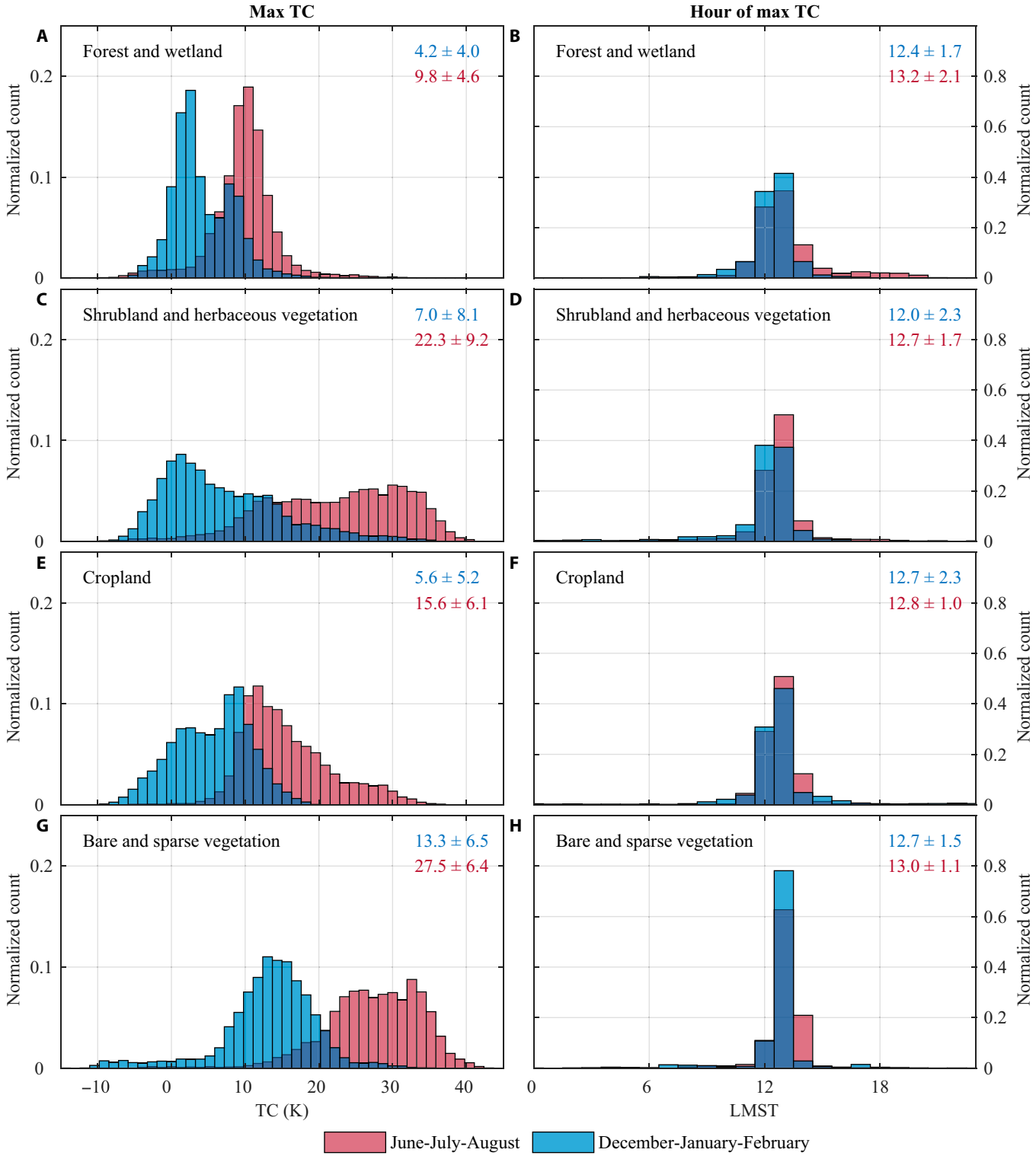

Fig. 10. The histograms in (A), (C), (E), and (G) show the distribution of maximum TC calculated at half PBL for different land cover types between 30°N and 60°N, for the selected periods of JJA and DJF. The histograms in (B), (D), (F), and (H) show the distributions of the LMST hour at which these maxima are reached. Mean and standard deviations are indicated on the top right.

addition, extended daylight hours in the summer lead to a longer daytime window with positive TCs. The TC measured at the height corresponding to the maximum temperature of the lower troposphere (MaxT, dashed lines) shows that the best nighttime measurements are on average in the autumn and winter. Negative TCs are observed after sunset, and show little variation throughout the night, even though on average an ever so slight decrease can be observed until sunrise. Although the magnitude of negative TCs varies little seasonally, the time window for potential nighttime measurements is substantially longer in winter than in spring and summer.

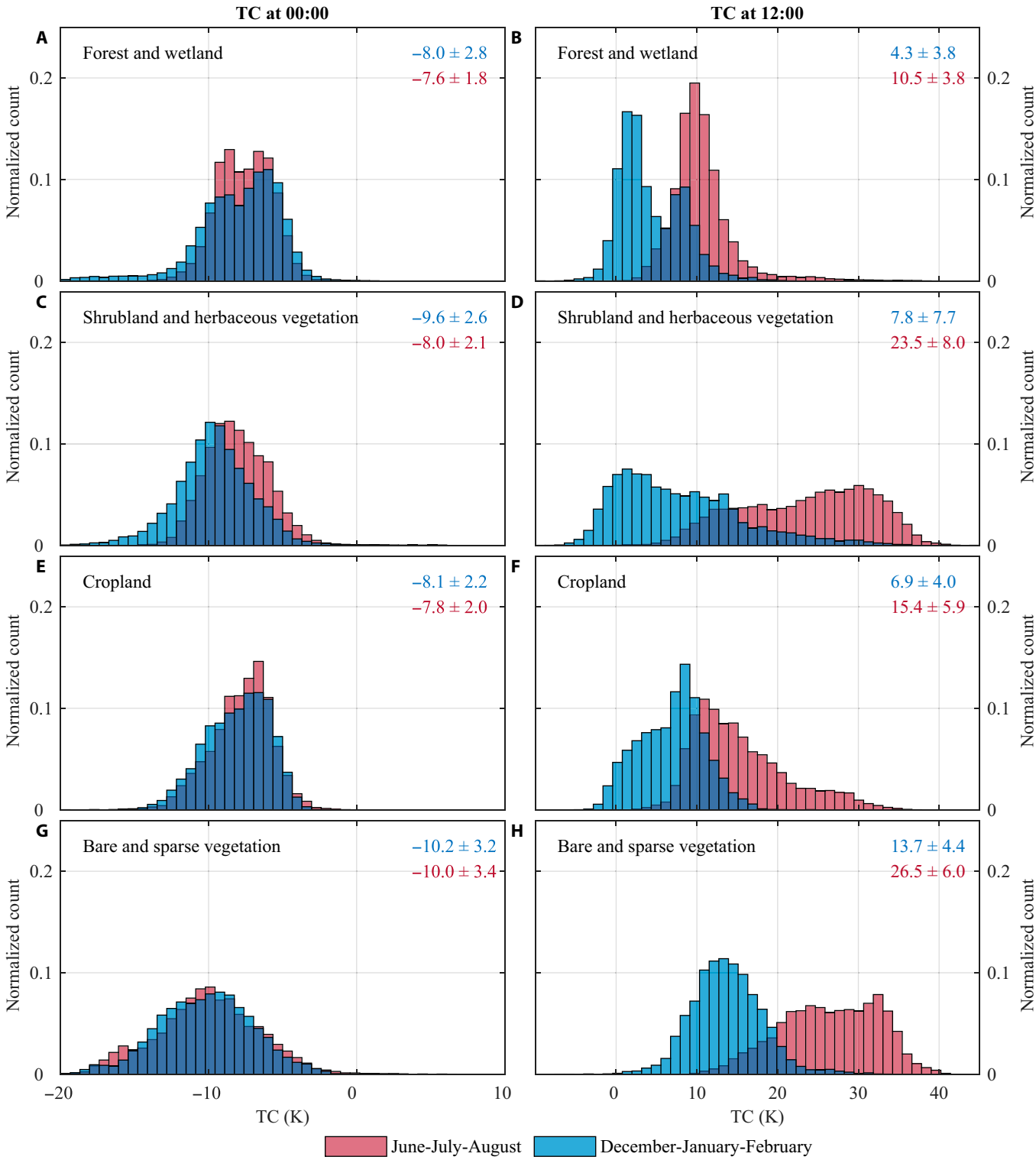

Fig. 11. Histograms of TC at 0000 LMST (A, C, E, and G) and 1200 LMST (B, D, F, and H) calculated at the height of the maximum temperature and half the PBL, respectively, for different land cover types, between 30°N and 60°N and for the selected periods of JJA and DJF. Mean and standard deviations are indicated on the top right.

Among the different land cover types, the smallest absolute TC values are found over forest and wetland. This land cover type is characterized by high soil moisture and an important amount of vegetation, which reduces the magnitude of the diel variations in surface temperature compared to other surface types due to cooling associated with evapotranspiration and evaporation [7,21,23]. Even in the summer, TCs never exceed 10 K. The measurement sensitivity of infrared sounders over this surface type is therefore generally weak. In practice, this poses a challenge to measure, e.g., biogenic emissions of volatile organic compounds in the lower part of the troposphere [37].

On the other end of the TC spectrum is the bare and sparse vegetation land cover type [7,20], which includes most large deserts. Sand and dry soils have a much lower heat capacity than water or vegetation and therefore heat up and cool down more quickly [21]. Average maxima reach almost 30 K, while the minima drop below −10 K. Comparable characteristics are observed for the shrubland and herbaceous vegetation land cover type. This land cover type is defined by a plant coverage above 4% for at least 2 months of the year [36], and thus includes a large part of bare soil as well. It encompasses, e.g., most of Australia and south-west US. Here, daily maxima are observed around 23 K in the summer, while the minima reach −9 K in the winter.

The cropland land cover type is intermediate in terms of measurement sensitivity. The maxima for this land cover type occur during spring (see further), reaching around 15 K. For the built-up land cover type (not shown) average maxima TC show results similar to cropland. One would expect larger TCs in the built up areas due to the fact that paved areas heat up more quickly than cropland. This was verified to be true on the metropolitan areas of Paris and Chicago, where the surface temperature in the built-up area was found to be some 5 K larger than that of the surrounding cropland. The fact that this is not seen in the average TC is likely a statistical effect related to the uneven distribution of built-up areas versus cropland in the considered latitude band. In fact, at the horizontal resolution of the dataset, the cropland type includes a lot of built up area.

Figure 10 provides histograms with the distribution of TC maxima and the LMST at which these occur, calculated at half the PBL, for the June-July-August (JJA) and December-January-February (DJF) seasons. As we are analyzing the northern hemisphere, these correspond respectively to summer and winter. Land cover types with little vegetation exhibit the largest scatter and strongest seasonal TC variability. The LMST histograms confirm that TC reaches its maximum between 1130 and 1330, consistent across all land cover types, with more than 80% of the observations falling into this time window. Figure 11 illustrates the distribution of TC at 0000 and 1200 LMST. The TC at 1200 shows results comparable to the distribution of TC maxima. The TC at 0000 shows very little seasonal variability, indicating that land cover and not season is the largest driver of TC at night. Bare and sparse vegetation stand out because of their large negative TC at night.

Figure 12 illustrates the monthly evolution of the TC in 2021, as before, at half of the PBL at 1200 (solid lines) and at the height of the maximum tropospheric temperature at 0000 (dashed lines). Both the average TC and the maximum (for the daytime) or minimum (for the nighttime) TC are shown. A large seasonal cycle is evident in the daytime values, with a clear difference in the maxima between bare and sparse

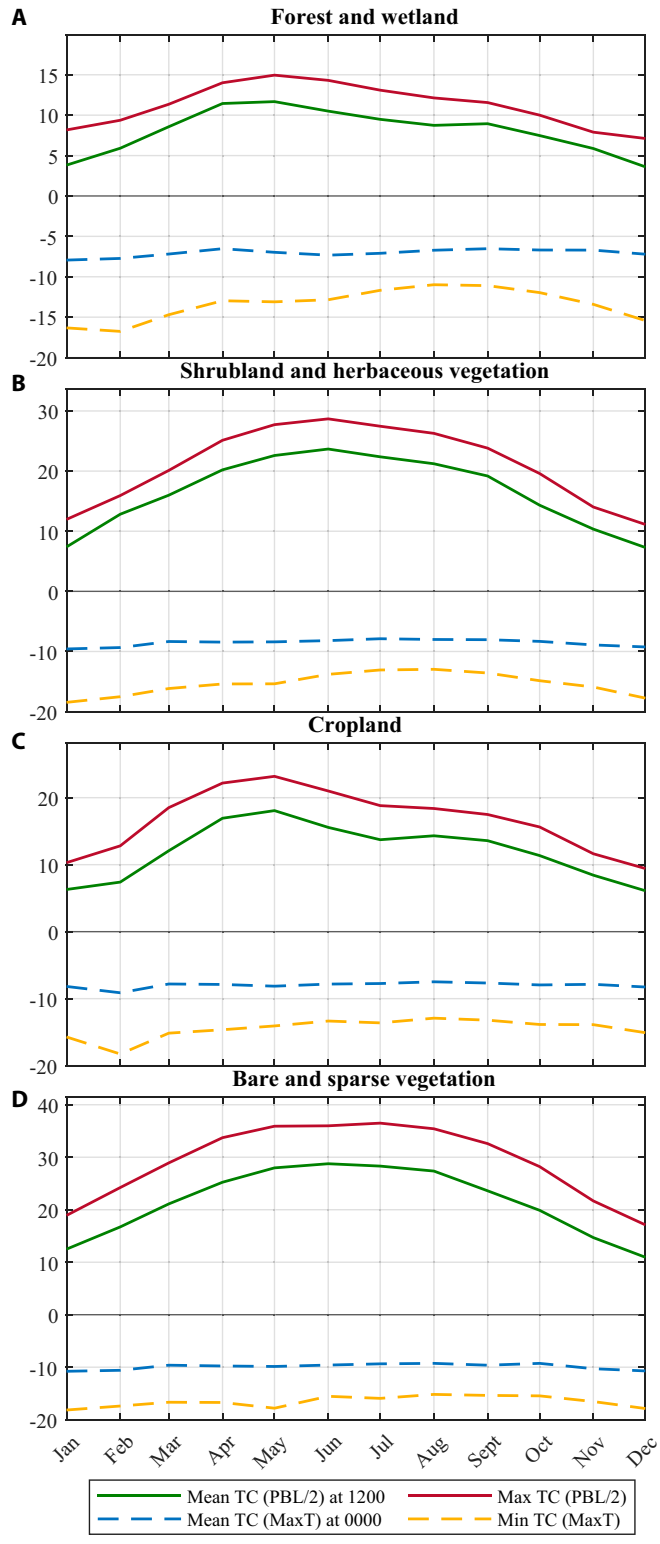

Fig. 12. Monthly TC averages for different land cover types (A to D) between 30°N and 60°N. The solid lines depict mean and maximum values of TC measured at half the PBL, while the dashed lines depict monthly mean and minima TC measured at the height corresponding to the maximum tropospheric temperature.

vegetation and between shrubland and herbaceous vegetation, which peak in May–July, and cropland as well as forest and wetland, which peak in April–May. The earlier peak, seen especially for cropland, might be due to increased vegetation cover in the summer, reducing its TC compared to that of spring. The monthly maxima are consistently about 2 to 8 K larger than the monthly averages.

At night, there is almost a complete absence of seasonality in the average TC across all land cover types. However, when looking at the averaged minimum TCs, a clear seasonal variation is exposed, with the most favorable observation conditions occurring in winter. This is especially marked for forest and wetland as well as cropland. The minima are caused by surface based temperature inversions that are much stronger but not more frequent in winter than in the other seasons [26].

Detection of NH_3 over the Po Valley

We conclude our analysis with an illustration of the measurement sensitivity over the Po Valley. It serves to make some important points, particularly on subtleties related to negative TC and temperature inversions, which are more difficult to convey in large-scale averages. Figure 13A shows the monthly averages and extremes of the hyperspectral range index (HRI) of NH_3 [15,18,38] observed over the Po Valley for IASI's morning and evening overpasses. The HRI quantifies the magnitude of NH_3 spectral signatures, with a positive HRI indicating absorption, and a negative HRI indicating emission. By definition, the HRI of spectra without detectable NH_3 have a mean of zero and a standard deviation of 1. Note that the HRI time series, as a measure of signal strength, convolves both the TC and NH_3 seasonality (similar to the left side of Eq. 4). The observed daytime seasonality shows enhanced HRI values throughout spring, summer, and autumn, and very little detectable NH_3 in winter, consistent with both the expected TC and NH_3 seasonality. The nighttime plot exhibits 2 clear periods with enhanced HRIs, one in late winter and another in autumn. The low HRIs, in absolute terms, observed in December and January are likely not a result of poor measurement sensitivity (low TCs) but can be attributed to low NH_3 concentrations. This is consistent with in situ observations and the fact that fertilizer application is generally prohibited in those months. In the late winter and autumn, negative TCs, together with the presence of enhanced NH_3 columns (due to, e.g., manure spreading, which typically takes place in those time periods [39]) result in negative average HRIs. Interestingly, before mid-March, the nighttime provides better measurement conditions for NH_3 than the daytime. The plot also shows the occurrence of very large negative HRIs on single days over the Po Valley, caused by large temperature inversions that coincide with large NH_3 columns.

The absence of negative HRIs during the warmer months is initially somewhat surprising, as the seasonal characterization that was presented before indicates on average an almost constant negative TC throughout the year. It can be explained by the NH_3vertical profile over the Po Valley during the warmer months: during daytime, NH_3 is mixed throughout the boundary layer, which in the summer extends well above 1,500 m compared to 200 to 600 m in late winter (see Fig. 13B). At 2130, the overpass time of IASI, there is likely still a large amount of background NH_3 present at high altitude in spring and summer, leading to a cancellation effect of spectral emission

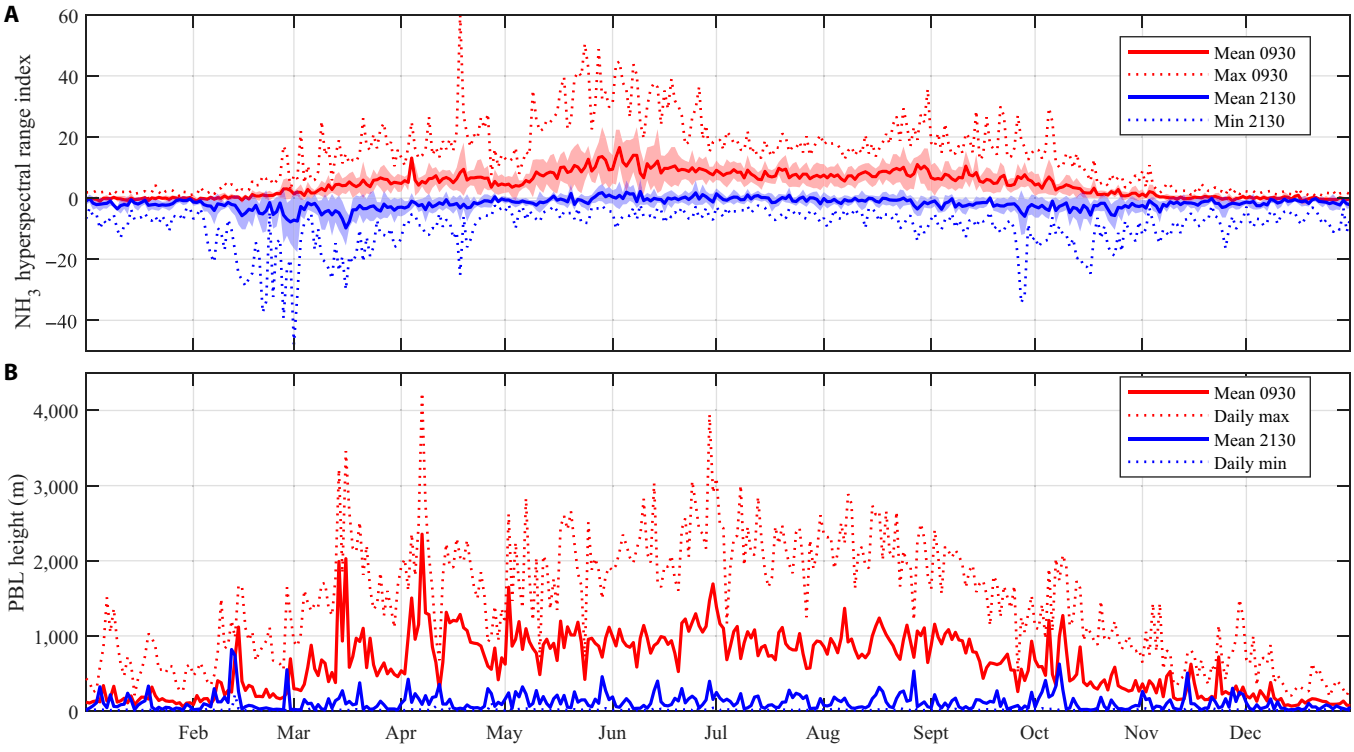

Fig. 13. Panel (A) shows the average NH_3 hyperspectral range index (HRI) measured over the Po Valley between 2011 and 2020 for IASI's morning and evening overpasses. The mean (solid), minimum and maximum (dotted) values of the HRI are shown during the morning overpass (around 0930) and evening overpass (around 2130). The filled area represents the standard deviation around the mean values. Panel (B) displays the daily PBL height over the Po Valley throughout the year 2021 during IASI's morning and evening overpasses. The solid lines represent the mean values of the PBL height, while the dotted lines represent the daily maxima and minima heights.

in the lowest layer of the atmosphere and absorption higher up. This illustrates that TC at a fixed altitude is only a proxy for measurement sensitivity at that altitude, whereas the sensitivity to the entire tropospheric column depends on the full vertical profiles of both the species of interest and the atmospheric temperature.

Conclusions

We started this paper with an overview of TC, how it originates in the lowest layers of the atmosphere, and how it drives measurement sensitivity of infrared nadir sounders. In the second part of the paper, we presented a global, year-long dataset of clear-sky TC at 3 different altitudes that can be used for a range of infrared remote sensing applications. The dataset enables evaluation of the seasonal and spatial variability of TC, revealing marked differences in daily maxima and minima of TC across different altitudes, latitudes, seasons, and land cover types. The dataset's high temporal resolution (1 h) enables an intraday assessment of the measurement sensitivity for current and future infrared sounders. Its high spatial resolution (31 km) reveals substantial local variability that can be exploited in regional studies.

We demonstrated that the optimal daytime measurement window for infrared sounders to detect near-surface pollutants consistently falls between 1130 and 1330 LMST in the spring and summer, depending on the land cover type. Variability of negative TC is driven by the duration of the night and land cover. Wintertime is the more favorable period for nighttime measurements when considering the maximum tropospheric temperature as a reference height. Finally, as illustrated on the Po Valley, depending on the vertical profile of the species of interest, large winter and autumn time inversions can lead to very favorable measurement conditions.

Acknowledgments

Funding: The study received funding from the Belgian State Federal Office for Scientific, Technical and Cultural Affairs (Prodex HIRS) and the Air Liquide Foundation (TAPIR project). Additionally, this work is supported by the FED-tWIN project ARENBERG ("Assessing the Reactive Nitrogen Budget and Emissions at Regional and Global Scales"), funded through the Belgian Science Policy Office (BELSPO). L.C. is a Research Associate supported by the Belgian F.R.S.-FNRS. L.N. acknowledges support from a FRIA (Fund for scientific Research in Industry and Agriculture) grant from the Belgian F.R.S-FNRS.
Author contributions: T.D.G. and L.C. analyzed the data and wrote the first version of the manuscript. T.D.G. prepared the figures. L.N. analyzed the NH_3 HRIs over the Po Valley. All authors participated in interpretation of the data, discussion, and revision of the manuscript.
Competing interests: The authors declare that there is no conflict of interest regarding the publication of this article.

Data Availability

The TC datasets are available at https://doi.org/10.5281/zenodo.10054376 [40].

References

1. McDuffie EE, Smith SJ, O'Rourke P, Tibrewal K, Venkataraman C, Marais EA, Zheng B, Crippa M, Brauer M, Martin RV. A global anthropogenic emission inventory of atmospheric pollutants from sector- and fuel-specific sources (1970–2017): An application of the community emissions data system (CEDS). *Earth Syst Sci Data*. 2020;12(4):3413–3442.
2. Beirle S, Borger C, Jost A, Wagner T. Improved catalog of NO2 point source emissions (version 2). *Earth Syst Sci Data*. 2023;15(7):3051–3073.
3. Fioletov VE, Mclinden CA, Griffin D, Abboud I, Krotkov N, PJT L, Li C, Joiner J, Theys N, Carn S. Version 2 of the global catalogue of large anthropogenic and volcanic SO2 sources and emissions derived from satellite measurements. *Earth Syst Sci Data*. 2023;15:75–93.
4. Lauvaux T, Giron C, Mazzolini M, d'Aspremont A, Duren R, Cusworth D, Shindell D, Ciais P. Global assessment of oil and gas methane ultraemitters. *Science*. 2022;375(6580):557–561.
5. Bauduin S, Clarisse L, Clerbaux C, Hurtmans D, Coheur PF. IASI observations of sulfur dioxide (SO2) in the boundary layer of Norilsk. *J Geophys Res Atmos*. 2014;119(7):4253–4263.
6. Bauduin S, Clarisse L, Hadji-Lazaro J, Theys N, Clerbaux C, Coheur PF. Retrieval of near surface sulfur dioxide SO2 concentrations at a global scale using IASI satellite observations. *Atmos Meas Tech*. 2016;9(2):721–740.
7. Deeter M, Edwards D, Gille J, Drummond J. Sensitivity of MOPITT to carbon monoxide in the lower troposphere. *J Geophys Res*. 2007;112(D24): https://doi.org/10.1029/2007JD008929
8. Bauduin S, Clarisse L, Theunissen M, George M, Hurtmans D, Clerbaux C, Coheur PF. IASI's sensitivity to near-surface carbon monoxide (CO): Theoretical analyses and retrievals on test cases. *J Quant Spectrosc Radiat Transf*. 2017;189:428–440.
9. Van Damme M, Clarisse L, Whitburn S, Hadji-Lazaro J, Hurtmans D, Clerbaux C, Coheur P-F. Industrial and agricultural ammonia point sources exposed. *Nature*. 2018;564(7734):99–103.
10. Clarisse L, Van Damme M, Clerbaux C, Coheur PF. Tracking down global NH3 point sources with wind-adjusted superresolution. *Atmos Meas Tech*. 2019;12(10):5457–5473.
11. Franco B, Clarisse L, Van Damme M, Hadji-Lazaro J, Clerbaux C, Coheur PF. Ethylene industrial emitters seen from space. *Nat Commun*. 2022;13:6452.
12. Stull R. *An introduction to boundary layer meteorology*. Dordrecht (The Netherlands): Kluwer Academic Publishers; 1988.
13. Clarisse L, Shephard MW, Dentener F, Hurtmans D, Cady-Pereira K, Karagulian F, van Damme M, Clerbaux C, Coheur PF. Satellite monitoring of ammonia: A case study of the San Joaquin Valley. *J Geophys Res*. 2010;115(D13): https://doi.org/10.1029/2009JD013291
14. Eremenko M, Sgheri L, Ridolfi M, Cuesta J, Costantino L, Sellitto P, Dufour G. Tropospheric ozone retrieval from thermal infrared nadir satellite measurements: Towards more adaptability of the constraint using a self-adapting regularization. *J Quant Spectrosc Radiat Transf*. 2019;238:106577.
15. Clarisse L, Van Damme M, Hurtmans D, Franco B, Clerbaux C, Coheur PF. The diel cycle of NH3 observed from the FY-4A geostationary interferometric infrared sounder (GIIRS). *Geophys Res Lett*. 2021;48(14):e2021GL093010.

16. Yurganov L, Carroll D, Pnyushkov A, Polyakov I, Zhang H. Ocean stratification and seaice cover in Barents and Kara seas modulate sea-air methane flux: Satellite data. *Adv Polar Sci*. 2021;32(2):118–140.
17. Noppen L, Clarisse L, Tack F, Ruhtz T, Merlaud A, Damme MV, Roozendael MV, Schuettemeyer D, Coheur P. Constraining industrial ammonia emissions using hyperspectral infrared imaging. *Remote Sens Environ*. 2023;291:113559.
18. Clarisse L, Franco B, Van Damme M, Di Gioacchino T, Hadji-Lazaro J, Whitburn S, Noppen L, Hurtmans D, Clerbaux C, Coheur P. The IASI NH3 version 4 product: Averaging kernels and improved consistency. *Atmos Meas Tech*. 2023;16(21):5009–5028.
19. Good EJ. An in situ-based analysis of the relationship between land surface "skin" and screen level air temperatures. *J Geophys Res Atmos*. 2016;121(15):8801–8819.
20. Good EJ, Ghent DJ, Bulgin CE, Remedios JJ. A spatiotemporal analysis of the relationship between near-surface air temperature and satellite land surface temperatures using 17 years of data from the ATSR series. *J Geophys Res Atmos*. 2017;122(17):9185–9210.
21. Prigent C, Aires F, Rossow W. Land surface skin temperatures from combined analysis of microwave and infrared satellite observations for an all-weather evaluation of the differences between air and skin temperatures. *J Geophys Res*. 2003;108(D10): https://doi.org/10.1029/2002JD002301
22. Hersbach H, Bell B, Berrisford P, Hirahara S, Horányi A, Muñoz-Sabater J, Nicolas J, Peubey C, Radu R, Schepers D, et al. The ERA5 global reanalysis. *Quart J Roy Meteorol Soc*. 2020;146(730):1999–2049.
23. Jin M, Dickinson R, Vogelmann A. A comparison of CCM2-BATS skin temperature and surface-air temperature with satellite and surface observations. *Am Meterol Soc*. 1997;10:1505–1524.
24. Petty GW. *A first course in atmospheric radiation*. Madison (WI): Sundog Publishing; 2006.
25. Clerbaux C, Boynard A, Clarisse L, George M, Hadji-Lazaro J, Herbin H, Hurtmans D, Pommier M, Razavi A, Turquety S, et al. Monitoring of atmospheric composition using the thermal infrared IASI/MetOp sounder. *Atmos Chem Phys*. 2009;9(16):6041–6054.
26. Palarz A, Celiński-Mysław D, Ustrnul Z. Temporal and spatial variability of surface-based inversions over Europe based on ERA-Interim reanalysis. *Int J Climatol*. 2018;38(1):158–168.
27. Huang Q, Chu Y, Li Q. Climatology of low-level temperature inversions over China based on high-resolution radiosonde measurements. *Theor Appl Climatol*. 2021;144:415–429.
28. Gentemann CL, Donlon CJ, Stuart-Menteth A, Wentz FJ. Diurnal signals in satellite sea surface temperature measurements. *Geophys Res Lett*. 2003;30(3):1140.
29. Clarisse L, Clerbaux C, Franco B, Hadji-Lazaro J, Whitburn S, Kopp AK, Hurtmans D, Coheur PF. A decadal data set of global atmospheric dust retrieved from IASI satellite measurements. *J Geophys Res*. 2019;124(3):1618–1647.
30. ECMWF. ECMWF Reanalysis v5 (ERA5) hourly data on single levels from 1940 to present, [dataset]. 2023. url: 10.24381/cds.adbb2d47
31. ECMWF. ECMWF Reanalysis v5 (ERA5) hourly data on pressure levels from 1940 to present, [dataset]. 2023. doi: 10.24381/cds.bd0915c6
32. Freitas SC, Trigo IF, Macedo J, Barroso C, Silva R, Perdigão R. Land surface temperature from multiple geostationary satellites. *Int J Remote Sens*. 2013;34:3051–3068.
33. Copernicus Global Land Service. Land Surface Temperature [dataset]. Last access: 28 October 2023. 2023. https://land.copernicus.eu/global/products/lst
34. Zhou DK, Larar AM, Liu X. MetOp-A/IASI observed continental thermal IR emissivity 464 variations. *IEEE J. Sel. Topics Appl. Earth Observ Remote Sens*. 2013;6:1156–1162.
35. Buchhorn M, Smets B, Bertels L, De Roo B, Lesiv M, Tsendbazar N-E, Herold M, Fritz S. Copernicus Global Land Service: Land Cover 100m: collection 3: epoch 2019: Globe, [dataset]. Version V3.0.1. 2020. doi: 10.5281/zenodo.3939050.
36. Jansen L, Di Gregorio A. *Land cover classification system (LCCS): Classification concepts and user manual*. Rome: FAO, 1998.
37. Franco B, Clarisse L, Stavrakou T, Müller JF, van Damme M, Whitburn S, Hadji-Lazaro J, Hurtmans D, Taraborrelli D, Clerbaux C, et al. A general framework for global retrievals of trace gases from IASI: Application to methanol, formic acid, and PAN. *J Geophys Res*. 2018;123(24):13963–13984.
38. Van Damme M, Clarisse L, Heald CL, Hurtmans D, Ngadi Y, Clerbaux C, Dolman AJ, Erisman JW, Coheur PF. Global distributions, time series and error characterization of atmospheric ammonia (NH3) from IASI satellite observations. *Atmos Chem Phys*. 2014;14(6):2905–2922.
39. Perego A, Basile A, Bonfante A, de Mascellis R, Terribile F, Brenna S, Acutis M. Nitrate leaching under maize cropping systems in Po Valley (Italy). *Agric Ecosyst Environ*. 2012;147:57–65.
40. Di Gioacchino T, Clarisse L, Noppen L, Van Damme M, Bauduin S, Coheur PF. Global monthly climatologies of thermal contrast. [dataset]. 2023. doi: 10.5281/ZENODO.10054376